FULL PAPER

Towards probing Earth's upper mantle with daily magnetic field variations: exploring a physics-based parametrization of the source

Géraldine Zenhäusern[1*] ⓘ, Alexey Kuvshinov[1], Martina Guzavina[1] and Astrid Maute[2]

Abstract

The electromagnetic (EM) field variations capable of probing the electrical conductivity of the upper mantle and mantle transition zone have a period range between a few hours and 1 day. At these periods, the dominant source of the EM signals is the ionospheric current system, which has a complex spatial and temporal structure. A concept of global-to-local (G2L) transfer functions can handle spatially complex source by relating global source expansion coefficients with locally measured magnetic (or/and electric) fields. When estimating the G2L transfer functions, the source is commonly expanded into spherical harmonics (SH). In this paper, we explore an alternative parametrization of the source based on a principal component analysis (PCA) of the Fourier transformed output from the physics-based Thermosphere Ionosphere Electrodynamics General Circulation Model (TIE-GCM). Specifically, we investigate whether magnetic fields computed in the realistic three-dimensional conductivity model of Earth excited by the PCA-based source agree better with observatory data than those computed in the same model but induced by the SH-based source. Using PCA to capture the source current compared to SH parametrization, we find that agreement with the observatory data is better during magnetically disturbed times and at shorter periods. Vice versa, it is poorer during magnetically quiet times and at longer periods.

Keywords: Electromagnetic induction, Ionospheric current systems, Magnetic field variations, Principal component analysis

Introduction

Geomagnetic depth sounding (GDS) uses a naturally time-varying electromagnetic (EM) field to constrain the conductivity distribution in the Earth's mantle. Using the derived conductivity distribution, the water, melt content, composition, and temperature distributions can be inferred. Of particular interest is the water content in the upper mantle (UM) and mantle transition zone (MTZ), as this parameter relates to Earth's dynamics. Fortunately, conductivity is especially sensitive to this. The periods of EM field variations sensitive to UM and

MTZ depths (0–670 km) are between a few hours and 1 day. This period range is dominated by daily EM field variations, which are mostly generated in the ionosphere, making them, however, challenging to use, because the ionospheric source has a spatially complex structure (e.g., Schmucker 1999; Guzavina et al. 2019).

At mid-latitudes, the prevailing signal in daily variations corresponds to solar-quiet (Sq) variations. These variations are produced on the sun-lit side of the Earth and caused by currents flowing in the ionosphere's E-region and lower F-region at the height of approximately 110 km (Maute and Richmond 2017b). The Sq current system is driven by solar tidal winds and, to a lesser extent, by lunar tides. This current system is generally described by a double vortex structure, one over each hemisphere. The northern current vortex rotates

*Correspondence: geraldine.zenhaeusern@erdw.ethz.ch
[1] Institute of Geophysics, ETH Zurich, Sonneggstrasse 5, 8092 Zurich, Switzerland
Full list of author information is available at the end of the article

Zenhäusern *et al. Earth, Planets and Space* (2021) 73:136

Page 2 of 16

anti-clockwise, while the southern vortex flows clockwise (Yamazaki et al. 2011). Sq variations manifest themselves most clearly during magnetically quiet periods (as indicated by their name) and at latitudes poleward of $\pm 5°$ of the dip equator and equatorward of $\pm 55°$ of the dipole latitude (Schmucker 1999). An additional current system is present within $\pm 5°$ of the dip equator, called the equatorial electrojet (EEJ). As the name implies, it is an intense current system flowing eastward along the dip equator and, same as Sq variations, present on Earth's sun-lit side. Its amplitude is significantly larger than Sq variations. While some view the currents as separate, others consider it as part of the Sq system (e.g., Olsen 1991; Yamazaki and Maute 2017). Here, EEJ is considered as part of the Sq system when discussing the different components of daily magnetic field variations. Poleward of $\pm 55°$ the auroral electrojet (AEJ) dominates. In contrast to the Sq current system, it is driven by the solar wind magnetospheric dynamo, which couples processes between the magnetosphere and the ionosphere (Yamazaki and Maute 2017; Alken et al. 2017). Magnetic field signals due to AEJ have a much larger amplitude than those due to the Sq current system and dominate the signal at high latitudes. The spatial structure of AEJ is different from Sq, but no less complex. In addition, its temporal structure is also more complex compared to Sq (Alken et al. 2017).

As Sq variations are produced predominately by solar tides, they vary daily, seasonally, with the solar cycle ($\sim$ 11 years), and on time scales longer than 11 years (Yamazaki and Maute 2017). The Sq system has the most hemispherically symmetric spatial structure during equinoctial months March and September. For the rest of the year, the vortexes are less symmetrical, since the southern (northern) hemisphere has a spatially larger vortex structure during northern (southern) winters (Chulliat et al. 2005).

One way to deal with spatially complex sources in GDS is to make use of a concept of global-to-local (G2L) transfer functions (TFs), which relate the locally measured magnetic (and electric, if available) field to global expansion coefficients describing the source (Püthe et al. 2015). This concept requires as adequate as possible description of the source. The Sq source's parameterization in the context of G2L TFs estimation has so far been based on the spherical harmonics (SH) expansion (Guzavina et al. 2019).

In this work, we explore an alternative parametrization based on spatial modes, which are estimated by principal component analysis (PCA) of the stream function obtained from a physics-based (PB) model of the ionosphere, specifically, the Thermosphere Ionosphere Electrodynamics General Circulation Model (TIE-GCM) (Qian et al. 2014).

Methods

Global-to-local transfer functions

Time-varying electric and magnetic fields are described by Maxwell's equations, which in the frequency domain are given by

$$\frac{1}{\mu_0} \nabla \times \vec{B} = \sigma \vec{E} + \vec{j}^{ext}$$
$$\nabla \times \vec{E} = -i\omega \vec{B}, \tag{1}$$

where μ_0 is the magnetic permeability of free space, $\sigma(\vec{r})$ the conductivity of the medium, ω the angular frequency, and $\vec{B}(\vec{r}, \omega)$ and $\vec{E}(\vec{r}, \omega)$ are the magnetic and electric fields, respectively. $\vec{j}^{ext}(\vec{r}, \omega)$ describes the extraneous current due to daily magnetic field variations. The position vector is defined as $\vec{r} = (r, \theta, \phi)$, where r, θ, ϕ are the distance from Earth's center, the colatitude, and the longitude in a geographic spherical coordinate system, respectively. At the desired periods, displacement currents can be neglected. If the extraneous current is surrounded by an insulator, thus including the non-conducting atmosphere below the ionosphere, it can be represented as a sheet current (Guzavina et al. 2019):

$$\vec{j}^{ext}(\vec{r}, \omega) = -\delta(r - b)\vec{e}_r \times \nabla_H \Psi(\Omega, \omega), \tag{2}$$

with δ Dirac's delta function, $b = a + h$, $a = 6371.2$ km is Earth's mean radius and h is the altitude at which the sheet current $\vec{j}^{ext}(\vec{r}, \omega)$ flows. This problem setup implies that we do not calculate the EM field inside the ionosphere. $\vec{e}_r$ is the radial unit vector of the spherical coordinate system, $\Omega = (\theta, \phi)$, and $\nabla_H \Psi$ denotes the tangential gradient of the stream function with

$$\nabla_H = \vec{e}_\theta \frac{1}{r} \frac{\partial}{\partial \theta} + \vec{e}_\phi \frac{1}{r \sin \theta} \frac{\partial}{\partial \phi}. \tag{3}$$

Following the approach by Guzavina et al. (2019), the stream function Ψ can be described as a linear combination of spatial modes:

$$\Psi(\Omega, \omega_p) = \sum_{l \in L^{PB}(p)} \epsilon_l(\omega_p) \Psi_l(\Omega), \tag{4}$$

where $L^{PB}(p)$ is the set of modes obtained from the physics-based approach describing the source at frequency ω_p. We consider $\omega_p = \frac{2\pi p}{T}$, where $p = 1, 2, .., 6$ is capped at the $6th$ time harmonic and $T = 24$ h. Combining Eq. (2) and Eq. (4), the extraneous current can be written as

$$\vec{j}^{ext}(\vec{r}, \omega_p) = \sum_{l \in L^{PB}(p)} \epsilon_l(\omega_p) \vec{j}_l(\vec{r}), \qquad (5)$$

where

$$\vec{j}_l(\vec{r}) = -\delta(r - b)\vec{e}_r \times \nabla_H \Psi_l(\Omega). \qquad (6)$$

Recalling Maxwell's equations then gives

$$\frac{1}{\mu_0} \nabla \times \vec{B}_l = \sigma \vec{E}_l + \vec{j}_l$$
$$\nabla \times \vec{E}_l = -i\omega_p \vec{B}_l. \qquad (7)$$

As Maxwell's equations are linear with respect to the source, the magnetic field can then be expressed as

$$\vec{B}(\vec{r}, \omega_p) = \sum_{l \in L^{PB}(p)} \epsilon_l(\omega_p) \vec{B}_l(\vec{r}, \omega_p). \qquad (8)$$

For comparison, the SH parametrization used by Guzavina et al. (2019) for the stream function is given as

$$\Psi(\vec{r}, \omega_p) = -\frac{a}{\mu_0} \sum_{n,m \in L^{SH}(p)} \frac{2n+1}{n+1} \left(\frac{b}{a}\right)^n \epsilon_n^m(\omega_p) S_n^m(\Omega). \qquad (9)$$

Similar to the PB parametrization, $L^{SH}(p)$ describes the set of terms using SH parametrization. The source $\vec{j}^{ext}$ is then written as

$$\vec{j}^{ext}(\vec{r}, \omega_p) = \sum_{n,m \in L^{SH}(p)} \epsilon_n^m(\omega_p) \vec{j}_n^m(\vec{r}), \qquad (10)$$

and

$$\vec{j}_n^m(\vec{r}) = \frac{\delta(r-b)}{\mu_0} \frac{2n+1}{n+1} \left(\frac{b}{a}\right)^{n-1} \vec{e}_r \times \nabla_\perp S_n^m. \qquad (11)$$

Here, n and m denote the degree and order of the spherical harmonic $S_n^m = P_n^{|m|}(\cos\theta)e^{im\phi}$, with $P_n^{|m|}$ the Schmidt quasi-normalised associated Legendre functions and $\nabla_\perp = r\nabla_H$. The double sum in Eq. (9) is given as (Schmucker 1999)

$$\sum_{n,m \in L^{SH}(p)} = \sum_{m=p-1}^{p+1} \sum_{n=m}^{m+3}. \qquad (12)$$

With this parametrization, Maxwell's equations for $\vec{j}_n^m$ can be written as

$$\frac{1}{\mu_0} \nabla \times \vec{B}_n^m = \sigma \vec{E}_n^m + \vec{j}_n^m$$
$$\nabla \times \vec{E}_n^m = -i\omega_p \vec{B}_n^m, \qquad (13)$$

and the magnetic field can be expressed as

$$\vec{B}(\vec{r}, \omega_p) = \sum_{n,m \in L^{SH}(p)} \epsilon_n^m(\omega_p) \vec{B}_n^m(\vec{r}, \omega_p). \qquad (14)$$

$\vec{B}_n^m$ and $\vec{B}_l$ both represent a set of global-to-local (G2L) "magnetic" transfer functions (TFs). They relate the global source coefficient ϵ_n^m (or ϵ_l, in the case of $\vec{B}_l$) to the locally measured magnetic field $\vec{B}$. In principle, one can obtain three TFs corresponding to each local magnetic field component. However, it is advantageous to use the (observed) tangential components only to estimate ϵ_n^m (or ϵ_l). This is due to a reduced sensitivity of the tangential components to the subsurface conductivity (Kuvshinov 2008). Furthermore, only the "radial" TF is estimated, relating the local radial component of the magnetic field with the pre-estimated ϵ_n^m (or ϵ_l). In the nomenclature of Püthe et al. (2015) this TF is denoted as T_n^m and reads

$$Z(\vec{r}, \omega_p) = \sum_{n,m \in L^{SH}(p)} \epsilon_n^m(\omega_p) T_n^m(\vec{r}, \omega_p), \qquad (15)$$

where $Z = -B_r$ and $T_n^m = -B_{n,r}^m$. In our case "radial" TFs are expressed as

$$Z(\vec{r}, \omega_p) = \sum_{l \in L^{PB}(p)} \epsilon_l(\omega_p) T_l(\vec{r}, \omega_p), \qquad (16)$$

where $T_l = -B_r^l$.

Obtaining spatial modes

To obtain the spatial modes introduced in Eq. (4), we use the stream function Ψ given by TIE-GCM. TIE-GCM is a numerical solver simulating the dynamics, composition, electrodynamics, and temperature of the coupled thermosphere–ionosphere system (Roble et al. 1988; Qian et al. 2014; Maute 2017). The TIE-GCM simulation employed in this study is described in Egbert et al. (2020), and the main points are repeated herein for context. The simulated ionospheric current has contributions from the neutral wind dynamo, gravity, and plasma pressure-gradient forcing (Maute and Richmond 2017a), and high-latitude magnetosphere–ionosphere coupling. The tidal and wave variability at the lower boundary of TIE-GCM (approximately at 97 km) is informed by 3-hourly Modern-Era Retrospective analysis for Research and Applications (MERRA) reanalysis data for the year 2009 (Häusler et al. 2010; Maute 2017). The magnetosphere–ionosphere coupling at high latitudes is simulated using empirical ion convection (Heelis et al. 1982) and auroral particle precipitation (Emery et al. 2012) patterns driven by the 3-hourly Kp index. The TIE-GCM simulation is conducted for the solar maximum conditions by using 2002 values for F10.7 and Kp. The full three-dimensional divergence-free ionospheric current
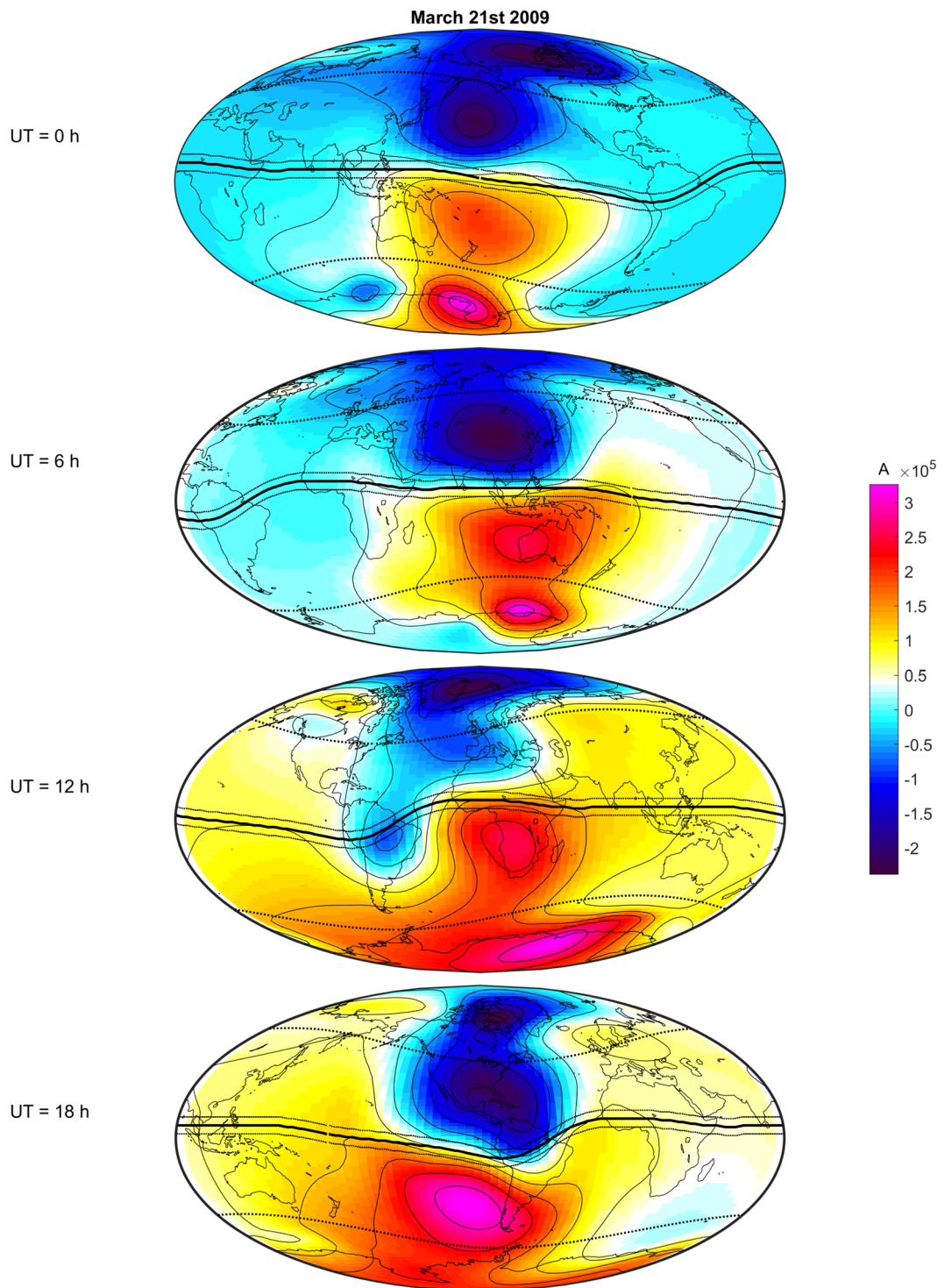
Zenhäusern *et al. Earth, Planets and Space*   *(2021) 73:136*

Page 4 of 16

Fig. 1 Time snapshots of TIE-GCM stream function $\Psi(t)$ on March 21 2009 (equinox)
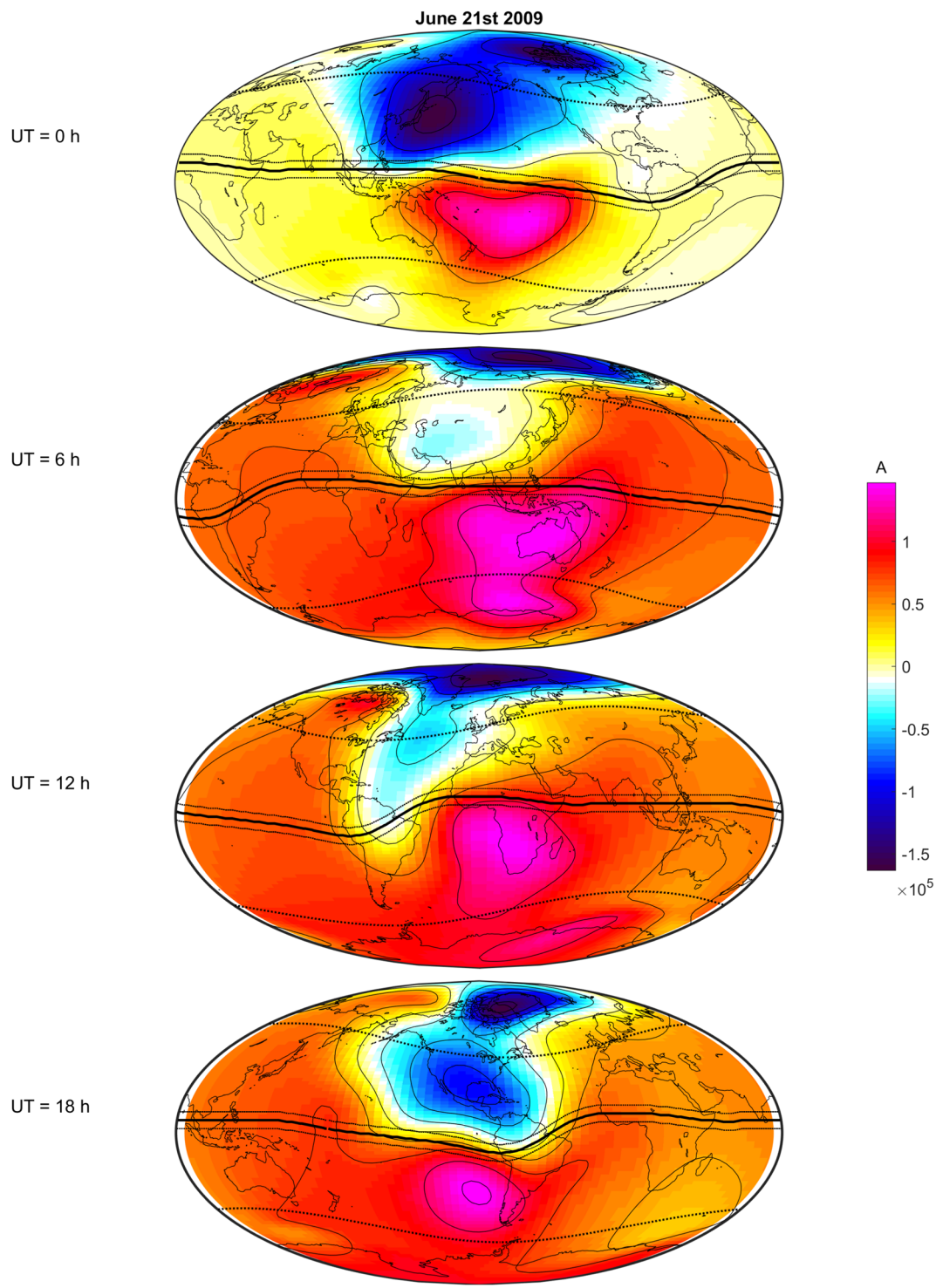
Fig. 2 Time snapshots of TIE-GCM stream function $\Psi(t)$ on June 21 2009 (solstice)

Zenhäusern *et al. Earth, Planets and Space* (2021) 73:136

Page 6 of 16

system and its associated magnetic perturbation is determined using a stand-alone electrodynamics module (Maute and Richmond 2017a). One of the outputs from this model is the desired stream function computed for the period between January 13th 01:00 and December 16th 24:00 2009 at a "coarse" $2° \times 5°$ grid with a sampling interval of 1 h. Examples of the TIE-GCM stream function for equinoctial and solstice days are presented in Figs. 1 and 2.

Since we will work in the frequency domain, TIE-GCM Ψ is first converted from the time to frequency domain by applying a Fourier transform (FT) to the Ψ time series at all grid points. The length of the time segment on which FT is applied is referred to as segment length s. The total number of non-overlapping segments S is given as $S = M/s$, where M is the time series' total length. We then construct a matrix F for each period ω_p as

$$
F(\omega_p) = \begin{pmatrix} \Psi_1^1(\omega_p) & \Psi_2^1(\omega_p) & \cdots & \Psi_N^1(\omega_p) \\ \Psi_1^2(\omega_p) & \Psi_2^2(\omega_p) & \cdots & \Psi_N^2(\omega_p) \\ \vdots & \vdots & \ddots & \vdots \\ \Psi_1^S(\omega_p) & \Psi_2^S(\omega_p) & \cdots & \Psi_N^S(\omega_p) \end{pmatrix}, \quad (17)
$$

where N is the number of grid points. Thus Ψ_i^j is the time-spectra estimate at the jth time segment at the ith grid point. Furthermore, according to the PCA concept, we form the covariance matrix R:

$$
R(\omega_p) = F(\omega_p)^H F(\omega_p) \quad (18)
$$

and apply to R an eigenvalue decomposition. Here, the superscript H denotes the Hermitian transpose. The eigenvectors represent the eigenmodes Ψ_l, or principal components (PCs), whereas the eigenvalues give the respective PC's variance contribution. The PCs are uncorrelated over space, as they are eigenvectors that are orthogonal to each other (Björnsson and Venegas 1997). They are usually sorted in order from the largest to the smallest eigenvalues. The PC corresponding to the largest eigenvalue will explain the most variance, followed by the second, third PC, etc. In practice, the PCs corresponding
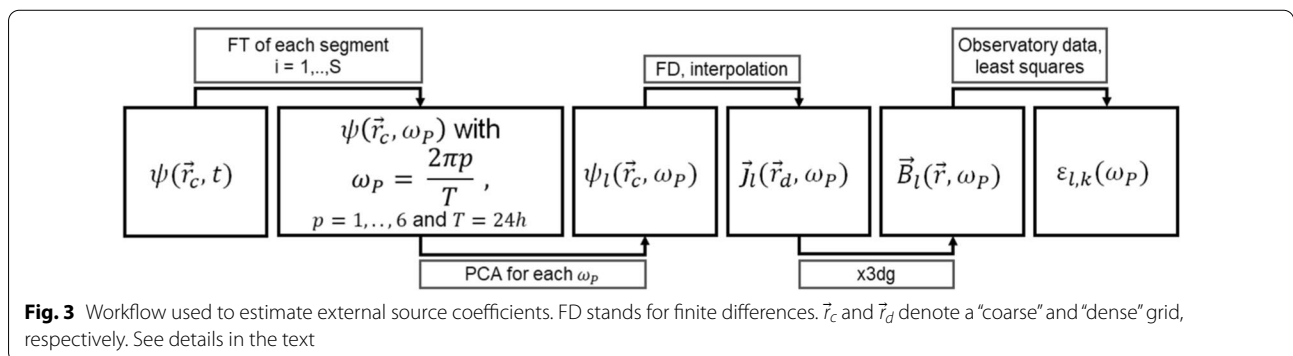
to a few of the largest eigenvalues explain most of the analyzed fields' variance. The cumulative variance of n PCs can be calculated as (e.g., Alken et al. 2017; Egbert et al. 2020)

$$
\kappa_n = \frac{\sum_{i=1}^{n} \lambda_i}{\sum_{i=1}^{N} \lambda_i}, \quad (19)
$$

where λ_i is the eigenvalue corresponding to ith PC, and N the total number of modes which in our case equals the number of grid points, i.e., $N = 90 \times 72 = 6480$. As it will be shown later in the paper, one needs at most 25 PCs (spatial modes) to explain more than 99% of the variance. This is a dramatic reduction from the total 6480 spatial modes. Moreover, even fewer modes are needed to achieve a meaningful agreement when fitting the data in practice. This will be discussed later in the paper.

Estimating external source coefficients

Figure 3 presents a workflow to estimate the external source coefficients, which are further used to assess the agreement with observatory data. Specifically, PCA is first applied to the output from the physics-based model. PCA is performed for different months and time series lengths to analyze the influence of different PCA setups on the resulting fit. Second, from the recovered modes $\Psi_l(\omega_p)$ (determined at a coarse, $2° \times 5°$, grid) the extraneous current $\vec{j}_l$ produced by each mode $1, 2, .., L^{PB}$ at period ω_p is calculated according to Eq. (6) using finite differences. The number of L^{PB} is investigated during the analysis and will be discussed later in the paper. Furthermore, $\vec{j}_l$ is interpolated at a finer, $1° \times 1°$, grid. The finer grid is required to compute the magnetic field $\vec{B}_l$ as accurate as feasible. The magnetic field computation relies on a numerical solution of Maxwell's equations given in Eq. (7). This is done with the use of the X3DG solver (Kuvshinov 2008) which is based on a volume integral equation approach with contracting kernel (cf. Pankratov and Kuvshinov 2016). The solver requires—along with $\vec{j}_l$—a

Fig. 3 Workflow used to estimate external source coefficients. FD stands for finite differences. $\vec{r}_c$ and $\vec{r}_d$ denote a "coarse" and "dense" grid, respectively. See details in the text

reference model of Earth's conductivity; here, the conductivity distribution described by Grayver et al. (2017) is used. Specifically, the conductivity model consists of a radially varying 1-D structure throughout the Earth with a layer of laterally varying conductance (of $1° \times 1°$ resolution) at the surface, accounting for the non-uniform distribution of the oceans and continents.

The external source coefficients ϵ_l described in Eq. (8) are calculated from the X3DG-derived tangential magnetic fields and the hourly-mean tangential magnetic fields from the global network of geomagnetic observatories. A detailed description of the observatory data used for the external coefficients' estimation can be found in Guzavina et al. (2019). Time spectra of the observatory magnetic fields are obtained at time harmonics of daily variations (i.e., at periods 24, 12, 8, 6, 4.8, and 4 h) for every day of the considered time interval. The source coefficients are estimated for the kth day ($k = 1, 2, ..., K$) and pth frequency ($p = 1, 2, ..., 6$) using a Huber-weighted robust regression method (Aster et al. 2018) as applied to the following minimization problem:

$$\left\| \mathbf{d}_k(\omega_p) - \mathrm{H}(\omega_p, \{\sigma\})\, \tilde{\epsilon}_k(\omega_p) \right\|_{\text{Huber}} \xrightarrow[\tilde{\epsilon}_k(\omega_p)]{} \min, \quad (20)$$

where k denotes the kth day, K is the number of days, $\mathbf{d}_k(\omega_p)$ is a data vector containing the pth time spectra of the observed tangential magnetic fields for the kth day, $\tilde{\epsilon}_k(\omega_p)$ is a vector with the estimated external source coefficients, and H is a matrix containing the predicted tangential magnetic fields. $\{\sigma\}$ denotes the 3-D conductivity distribution in the reference model described above. As an example, for $p = 1$ (period of 24 h), the corresponding vectors and matrix look as follows:

$$\begin{aligned} \mathbf{d}_k = (&X_k^{\text{obs}}(\vec{r}_1, \omega_1), \cdots, X_k^{\text{obs}}(\vec{r}_N, \omega_1), \\ &Y_k^{\text{obs}}(\vec{r}_1, \omega_1), \cdots, Y_k^{\text{obs}}(\vec{r}_N, \omega_1))^T, \end{aligned} \quad (21)$$

$$\tilde{\epsilon}_k = (\tilde{\epsilon}_{1,k}(\omega_1), \tilde{\epsilon}_{2,k}(\omega_1), \cdots, \tilde{\epsilon}_{L^{PB}(1),k}(\omega_1))^T, \quad (22)$$

Here, the superscript T denotes the transpose of a vector, $X = -B_\theta$ and $Y = B_\phi$ are north- and east-directed magnetic field components, respectively. Note that the number of geomagnetic observatories used for the external coefficients' estimation can be adjusted for their latitudinal position. In the paper, we explore two sets of observatory data: data from observatories from all latitudes and observatories with geomagnetic latitudes restricted to poleward of $\pm 5°$ and equatorward of $\pm 55°$. With the latter restrictions, the influence on the results of both the equatorial and auroral electrojets can be minimized.

Assessing the agreement with observatory data

To quantitatively assess the performance of different set-ups during the PCA analysis, we will use the coefficient of determination R^2, which is defined as

$$R_k^2(\mathcal{B}, \omega_p) = 1 - \frac{\sum_{j=1}^{N} |\mathcal{B}_k^{\text{obs}}(\vec{r}_j, \omega_p) - \mathcal{B}_k^{\text{pred}}(\vec{r}_j, \omega_p, \{\sigma\})|^2}{\sum_{j=1}^{N} |\mathcal{B}_k^{\text{obs}}(\vec{r}_j, \omega_p) - \overline{\mathcal{B}}_k^{\text{obs}}(\omega_p)|^2} \quad (24)$$

where $\vec{r}_j$ is the observatory location, $\mathcal{B}$ stands for either magnetic field component X, Y, or Z. $\overline{\mathcal{B}}$ is the mean of the observed magnetic field component over N used observatories at day k, and it is calculated as

$$\overline{\mathcal{B}}_k^{\text{obs}}(\omega_p) = \frac{1}{N} \sum_{j=1}^{N} \mathcal{B}_k^{\text{obs}}(\vec{r}_j, \omega_p). \quad (25)$$

The predicted fields are calculated as

$$\mathcal{B}_k^{\text{pred}}(\vec{r}_j, \omega_p, \{\sigma\}) = \sum_{l \in L^{PB}(p)} \epsilon_{l,k}(\omega_p) \mathcal{B}_l(\vec{r}_j, \omega_p, \{\sigma\}). \quad (26)$$

The closer this coefficient is to one, the better the accumulative (i.e., across all observatories) agreement between predicted and observed (i.e., estimated from the data) magnetic fields at the pth frequency/period.

$$H = \begin{pmatrix} X_1(\vec{r}_1, \omega_1, \{\sigma\}) & X_2(\vec{r}_1, \omega_1, \{\sigma\}) & \cdots & X_{L^{PB}(1)}(\vec{r}_1, \omega_1, \{\sigma\}) \\ X_1(\vec{r}_2, \omega_1, \{\sigma\}) & X_2(\vec{r}_2, \omega_1, \{\sigma\}) & \cdots & X_{L^{PB}(1)}(\vec{r}_2, \omega_1, \{\sigma\}) \\ \vdots & & & \\ X_1(\vec{r}_N, \omega_1, \{\sigma\}) & X_2(\vec{r}_N, \omega_1, \{\sigma\}) & \cdots & X_{L^{PB}(1)}(\vec{r}_N, \omega_1, \{\sigma\}) \\ Y_1(\vec{r}_1, \omega_1, \{\sigma\}) & Y_2(\vec{r}_1, \omega_1, \{\sigma\}) & \cdots & Y_{L^{PB}(1)}(\vec{r}_1, \omega_1, \{\sigma\}) \\ Y_1(\vec{r}_2, \omega_1, \{\sigma\}) & Y_2(\vec{r}_2, \omega_1, \{\sigma\}) & \cdots & Y_{L^{PB}(1)}(\vec{r}_2, \omega_1, \{\sigma\}) \\ \vdots & & & \\ Y_1(\vec{r}_N, \omega_1, \{\sigma\}) & Y_2(\vec{r}_N, \omega_1, \{\sigma\}) & \cdots & Y_{L^{PB}(1)}(\vec{r}_N, \omega_1, \{\sigma\}) \end{pmatrix}. \quad (23)$$

Zenhäusern *et al. Earth, Planets and Space*   (2021) 73:136

Page 8 of 16

Results and discussion

As Sq variations change not only daily but also seasonally, restricting PCA to a certain interval of the whole year, TIE-GCM output data can be used to capture some state of the Sq source. (As explained above, under TIE-GCM output data we understand the stream function computed for the period between January 13th 01:00 and December 16th 24:00 2009.) For example, the double vortex structure of Sq is most symmetric during the equinoctial months March–April and September–October; thus, the spatial modes obtained from only these months are hypothesized to represent the most simple spatial structure. Similarly, the solstice months June–July and December–January should represent the most complex Sq current system structure and should, therefore, require a larger number of spatial modes to explain the same amount of variance in the source.

The segment length s is another parameter that can be adjusted. As the Sq source varies predominantly daily, the obvious choice for s is 24 h. However, other non-periodic variations such as coming from the auroral electrojet are also captured within this segment length. As their amplitude is much larger than that of Sq variations at high latitudes, this may mask Sq in the spatial modes. By increasing s, the non-periodic contributions to the daily variations such as AEJ should be minimized, and the resulting modes should depict Sq variations more clearly.

Instead of using the original TIE-GCM stream function $\Psi(t)$, it is also possible to suppress smaller scale (but larger amplitude) signals coming from AEJ and EEJ. This can be done by applying a spherical harmonic filter with a specified cutoff degree. The resulting $\Psi_{filt}(t)$ should contain fewer short-wavelength features than the original stream function. This approach can be used to reduce the complexity of the source, as well as focus on large-scale features contained therein.

In the following sections, we will discuss how all the above-mentioned PCA setups influence the results.

Dependence of the results on period

We start with investigating how many spatial modes at each period are needed to explain most of the TIE-GCM stream function variability. Figure 4 presents the cumulative variance (cf. Eq. 19) for the first 30 spatial modes at each considered period. In this model experiment, all 338 days were used for PCA, and the segment length s was taken as 24 h. Dashed and dash-dotted horizontal lines allow us to estimate the number of modes needed to explain 95% and 99% of the TIE-GCM data variability, respectively. It is seen that this number varies noticeably with period. For periods in the range of 24–6 h, the tendency is apparent: the longer the period, the smaller the
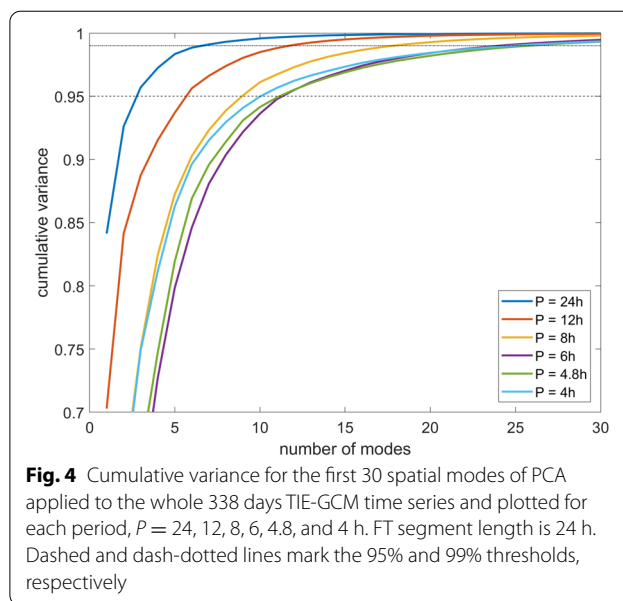
Fig. 4 Cumulative variance for the first 30 spatial modes of PCA applied to the whole 338 days TIE-GCM time series and plotted for each period, $P = 24, 12, 8, 6, 4.8$, and 4 h. FT segment length is 24 h. Dashed and dash-dotted lines mark the 95% and 99% thresholds, respectively

number of modes is required to explain the major part of variability. At periods 4.8 and 4 h, the number of "significant" (i.e., explaining the specified value of variability) modes, denoted hereinafter as N_{sign}, remains approximately the same as for the period of 6 h. This indicates that the source's complexity increases from 24 h to 6 h periods, after which it stays unchanged. The increase of the threshold for the explained variability from 95% and 99% expectedly leads to an increase in N_{sign}; de facto, the number of modes approximately doubles. Table 1 demonstrates quantitatively the above observations. The table also contains the results for PCA performed for a 2 months ("equinoctial") interval of TIE-GCM data, namely, for March and April (61) days. For this scenario, the number of N_{sign} appears to be two times smaller than when all 338 days are used for PCA. A decrease of N_{sign} is not totally surprising, since (almost) 1 year of TIE-GCM data should reveal (by construction) more stream function variance. We also expected that the structure of ionospheric source is less spatially complex during equinoctial months, which could also be the reason for a significant decrease in N_{sign} when only March and April data are used (cf. Alken et al. 2017).

Dependence of the results on the time interval used for PCA

As we saw in the previous section, the choice of time interval for PCA substantially affects N_{sign}. In this section, we explore this effect in more detail. Figure 5 presents N_{sign} with respect to period, season, and the length of used time interval. As expected, the shorter

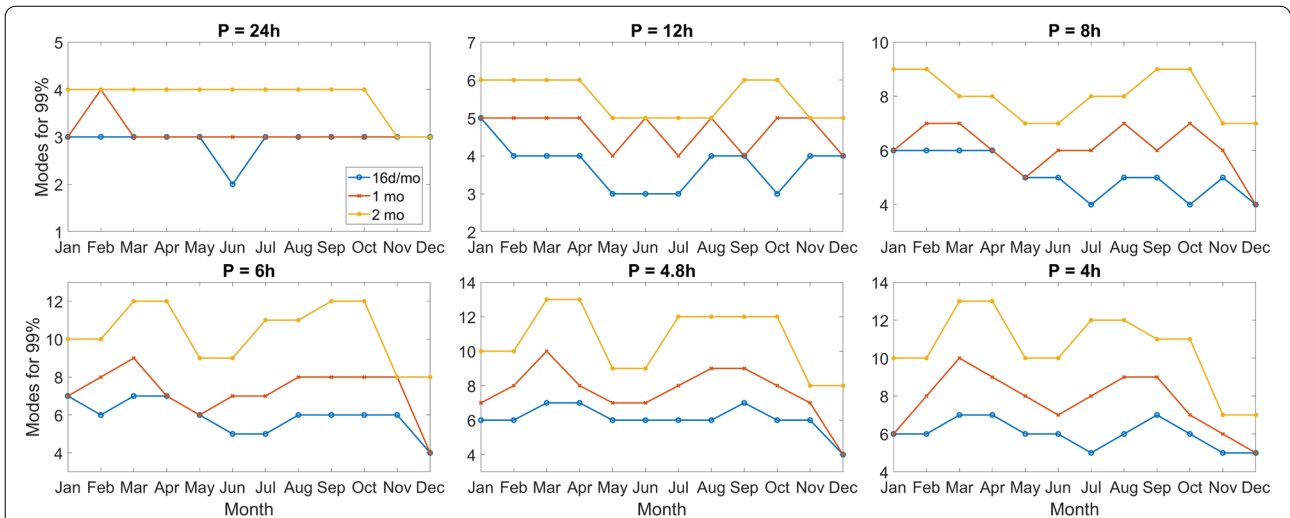Zenhäusern *et al. Earth, Planets and Space*   (2021) 73:136

Page 9 of 16

Fig. 5 Number of modes needed to explain 99% variance for each period, $P = 24, 12, 8, 6, 4.8,$ and 4 h. The time series length is 16 days, 1 month, and 2 months (adjacent months, thus January–February, March–April, May–June, etc.). The FT segment length for all PCA runs is 24 h. Note that January and December do not have the full months of data available, as the TIE-GCM stream function spans 13.01.2009-16.12.2009

Table 1 Table listing the number of spatial modes needed for each period to surpass either 95 or 99% variance (κ) threshold. The list includes PCA results using the full data set and restricting the data to March–April

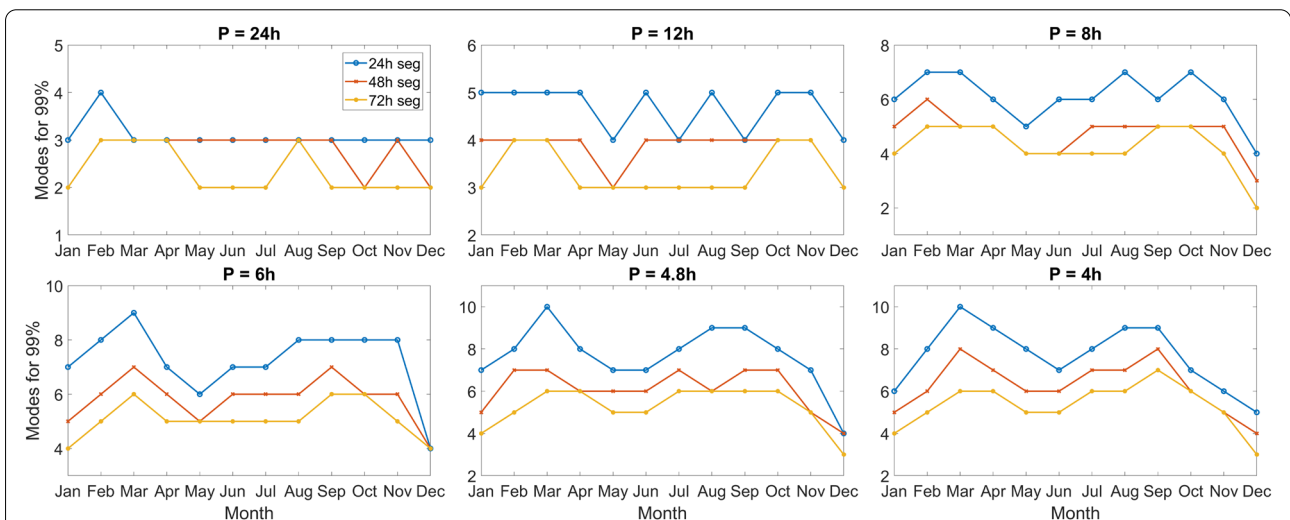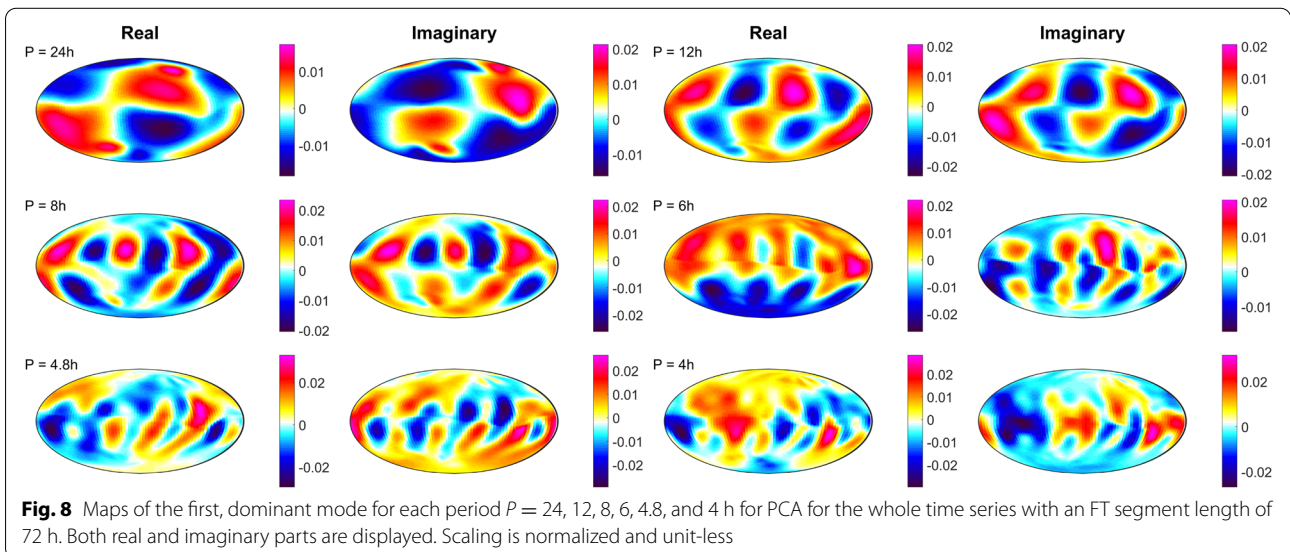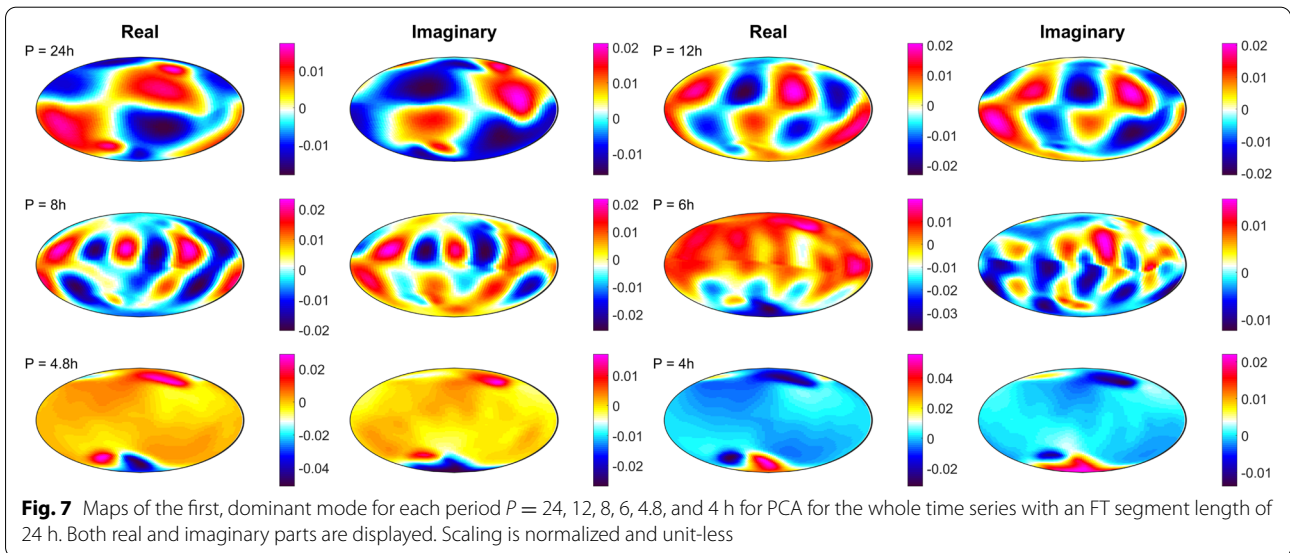| Time Series	κ [%]	Period [h]					
		24	**12**	**8**	**6**	**4.8**	**4**
Full year	95	3	6	9	12	12	11
	99	7	12	18	25	26	25
March–April	95	2	3	5	6	7	7
	99	4	6	8	12	13	13

Fig. 6 Number of modes needed to explain 99% variance for each period, $P = 24, 12, 8, 6, 4.8,$ and 4 h. The time series length is restricted to single months, and the FT segment length is varied between 24, 48, and 72 h. Note that January and December do not have the full months of data available, as the stream function spans 13.01.2009-16.12.2009

Zenhäusern *et al. Earth, Planets and Space*   (2021) 73:136

Page 10 of 16

time intervals require fewer modes to explain the variance. This effect can be seen at all periods; however, it is more pronounced at shorter periods. The figure illustrates again that more modes are needed to explain variance at shorter periods. The counter-intuitive result we obtain is that N_{sign} was the largest/smallest when we performed PCA for the equinoctial/solstice months data, opposite to our expectations; hitherto, we don't have an explanation for this result.

Dependence on the FT segment length

The length of the time segment on which the FT is applied also affects the results significantly. Figure 6

shows N_{sign} with respect to period and FT segment length. It is seen that the longer the FT segment, the smaller N_{sign}; this effect is observed at all periods. It is also instructive to look at the first (dominant) mode at each period using different FT segments. Figures 7 and 8 present these modes when PCA is performed for the whole year TIE-GCM data using FT segment lengths as 24 and 72 h, respectively. It is seen that the dominant modes at longer periods (6–24 h) are almost not affected by the length of the FT segment. This is not the case for the shortest periods of 4.8 and 4 h. With 24 h FT segments, the corresponding modes are dominated by high latitude features, most probably due to

Fig. 7 Maps of the first, dominant mode for each period P = 24, 12, 8, 6, 4.8, and 4 h for PCA for the whole time series with an FT segment length of 24 h. Both real and imaginary parts are displayed. Scaling is normalized and unit-less

Fig. 8 Maps of the first, dominant mode for each period P = 24, 12, 8, 6, 4.8, and 4 h for PCA for the whole time series with an FT segment length of 72 h. Both real and imaginary parts are displayed. Scaling is normalized and unit-less

Zenhäusern *et al. Earth, Planets and Space*   (2021) 73:136

Page 11 of 16

AEJ, and thus no (Sq) features are visible at lower latitudes. When increasing FT segments' length up to 72 h, high latitude structures no longer have the largest amplitude; mid-latitude features start to dominate and show the patterns one expects for the Sq signal. This indicates that the high latitude structures that dominate when using short FT segments are not periodic over multiple days and are thus filtered out when using longer segments.

High latitude spatial filtering

We also tried to diminish the influence of AEJ on the results by applying a spatial spherical harmonics filter to the TIE-GCM stream function, thus removing the short scale structures which are assumed to be associated with AEJ. The cutoff degree in the SH filtering, N_{cut}, varied from 6 to 18. However, our model experiments (not shown in the paper) show that such filtering does not lead to an improved agreement between observations and modeling results, as quantified by the coefficient of determination R^2 discussed previously.

We also tried some other PCA setups, but overall we did not notice that some specific setup provides an agreement between observations and modeling results, which can be considered noticeably outperforming. Table 2 summarizes the results of all model experiments we performed.

Comparison of the SH- and PCA-based results

Among all PCA results, the best agreement with the observed data, as given by the coefficient of determination R^2, is obtained using the whole year of data with 24 h FT segments. We compare the corresponding R^2 with those computed by exploiting SH parameterization of the source (Guzavina et al. 2019). Figures 9 and 10 show R^2 for tangential and vertical components, respectively. Note that Guzavina et al. (2019) used the same number (12) of SH terms to describe the source (with one exception, however: 11 terms for the period of 24 h). We also note that at each period Guzavina et al. (2019) used different sets of SH terms while keeping the same number of terms. It is seen that in comparison to SH parametrization, the PCA-based parameterization gives a better agreement with the observations at all components during magnetically disturbed times and at shorter periods. Conversely, the agreement is poorer during magnetically quiet times and at longer periods.

Finally, we compare—at selected geomagnetic observatories and for the period of 3 days—the observed magnetic fields with those predicted using the PCA-based and SH parametrization of the source. Figure 11 shows the results at observatories Alice Springs (ASP), Boulder (BOU), Chambon la Foret (CLF), and Honolulu (HON). Agreement between observed and predicted fields varies with components and observatories and is generally best on the *Y* component. From the figure, it is difficult to judge whether the predictions based on the physics (PCA)-based parameterization of the source are in a better agreement with observations than the "SH-based" predictions. Overall both predictions agree well with observations.

Table 2 Table listing the major findings of this work. The explored parameters are period P = 24, 12, 8, 6, 4.8, 4 h; variance σ^2 = 95% or 99% provided by PCA; total length of time series used for PCA (maximum—almost 1 year, minimum—2 weeks); selection of time series (separating them into sections); high latitude filtering by applying an SH filter of degree N_{cut}; segment length along which a Fourier transform is applied (24, 48, 72 h); and latitude of observatory stations used for the estimation of the source coefficient. "N/A" stands for not applicable

Explored parameter	Effect on the number of modes	Effect on the spatial features	R^2 results
Period (P)	Increases for decreasing P	Long P show larger scale features Short P show smaller and high latitude features	Increased agreement with increasing P
Variance	Doubles when going from 95 to 99%	Subsequent modes tend towards smaller scale features	Improved when using higher variance
Length of time series	Increases for longer time series	Only a weak effect on the dominant modes	Improved for longer time series
Selection of time series	Increases for equinoctial months	Only a weak effect on the dominant modes	Weak improvement for equinoctial months
High latitude filtering	Decreases (more prominent for lower N_{cut})	Features are blurred, but still present at high latitudes	Worsens compared to unfiltered data
FT segment length	Decreases for longer segment lengths	Longer segment lengths show expected Sq pattern at short P	Improved for short segment lengths
Observatory latitude	N/A	N/A	Best agreement using only mid latitudes

Zenhäusern *et al. Earth, Planets and Space* (2021) 73:136
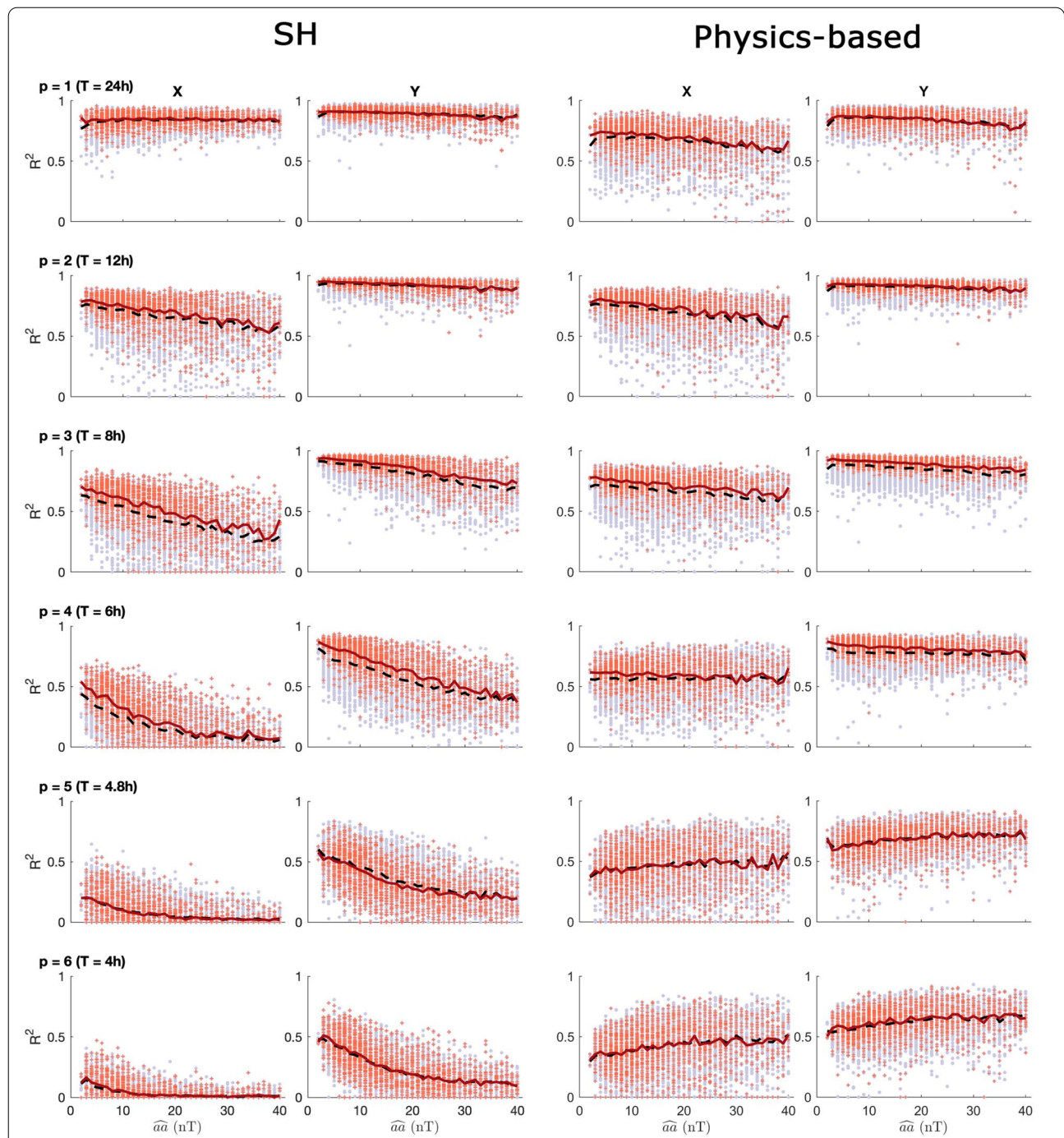
Page 12 of 16

Fig. 9 Coefficient of determination R^2 for periods $P =$ 24, 12, 8, 6, 4.8, and 4 h for magnetic field components X and Y. $X = -B_\theta$ and $Y = B_\phi$ denote the north and east components, respectively. Stations for estimating the Sq coefficients are limited to mid-latitudes between ±5° and 55°. Two leftmost columns: R^2 computed by Guzavina et al. (2019) using a spherical harmonic parameterization of the source. Two rightmost columns: R^2 computed using a PCA-based parameterization of the source. The number of modes corresponds to the 99% threshold for the variance of the TIE-GCM stream function. PCA was applied to the whole 338 days TIE-GCM time series. FT segment length was taken as 24 h. Grey circles mark all days, and red pluses mark equinoctial days. The lines mark their mean values, respectively. The *aa* index indicates the level of geomagnetic disturbance, where a larger index stands for a more disturbed day; more details about this index can be found in Guzavina et al. (2019)
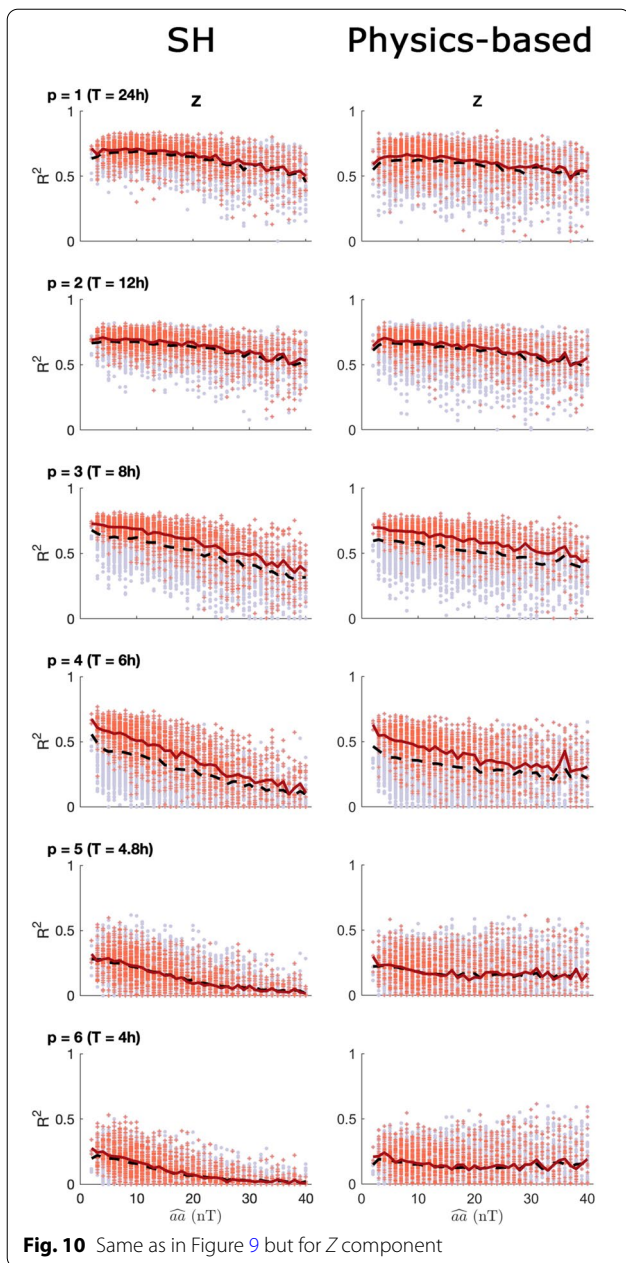
Fig. 10 Same as in Figure 9 but for *Z* component

(TIE-GCM). We tried different PCA setups to explore the behavior of the recovered PCA spatial modes.

One major finding is the period dependence of the PCA-based parametrization. We find that longer periods require fewer modes, and long-wavelength features expectedly dominate them. Short periods require more modes and show predominately short-wavelength structures. This dependency of daily magnetic signals on period could be used in other parametrization schemes as well. Note that previous studies based on SH parameterization (Koch and Kuvshinov 2013; Guzavina et al. 2018, 2019) have kept the number of SH terms constant for all periods. A more nuanced parametrization that considers the differences between periods might improve the results when estimating the external source coefficients, and in turn, may improve estimation of global-to-local transfer functions (Guzavina et al. 2019).

We find that the choice of FT segment length affects the resulting modes. The high latitude features dominating at short periods when using 24 h segments, caused by AEJ, vanish when using 72 h segments. Furthermore, it seems that limiting the time series which supplies the basis for PCA does not improve the fit with the observed data; this was based on the assumption that using only equinoctial months, which have the simplest spatial structure for Sq, would help stabilize the parametrization and thus reduce seasonal fluctuations. The best agreement with the observed data is achieved using modes obtained from the whole year of model data using 99% variance as a threshold and 24 h as segment length. Furthermore, the fit is better when latitudes are restricted to mid-latitudes, namely, poleward of $\pm 5°$ and equatorward of $\pm 55°$.

In contrast to using a SH parametrization to describe daily magnetic signals, PCA performs almost as good when using observatories from all latitudes compared to limiting them to mid-latitudes only. Therefore, a wider range of measurements is available, and possibly the conductivity beneath high latitude stations as well as stations located near the dip equator can be inferred. This can expand the available data significantly.

PCA performs better than SH at magnetically disturbed days, meaning with increased *aa* index. As SH struggles with increased magnetic disturbance, PCA seems to offer a suitable alternative for data containing many disturbed days.

We find that the physics-based parametrization performs worse than SH at $P = 24$ h. This could be due to the fact that TIE-GCM does not include effects from the magnetosphere and inner magnetosphere, e.g., from ring and tail currents, contributing to daily magnetic field variations. An alternative physics-based model, such as the Ground-to-topside model
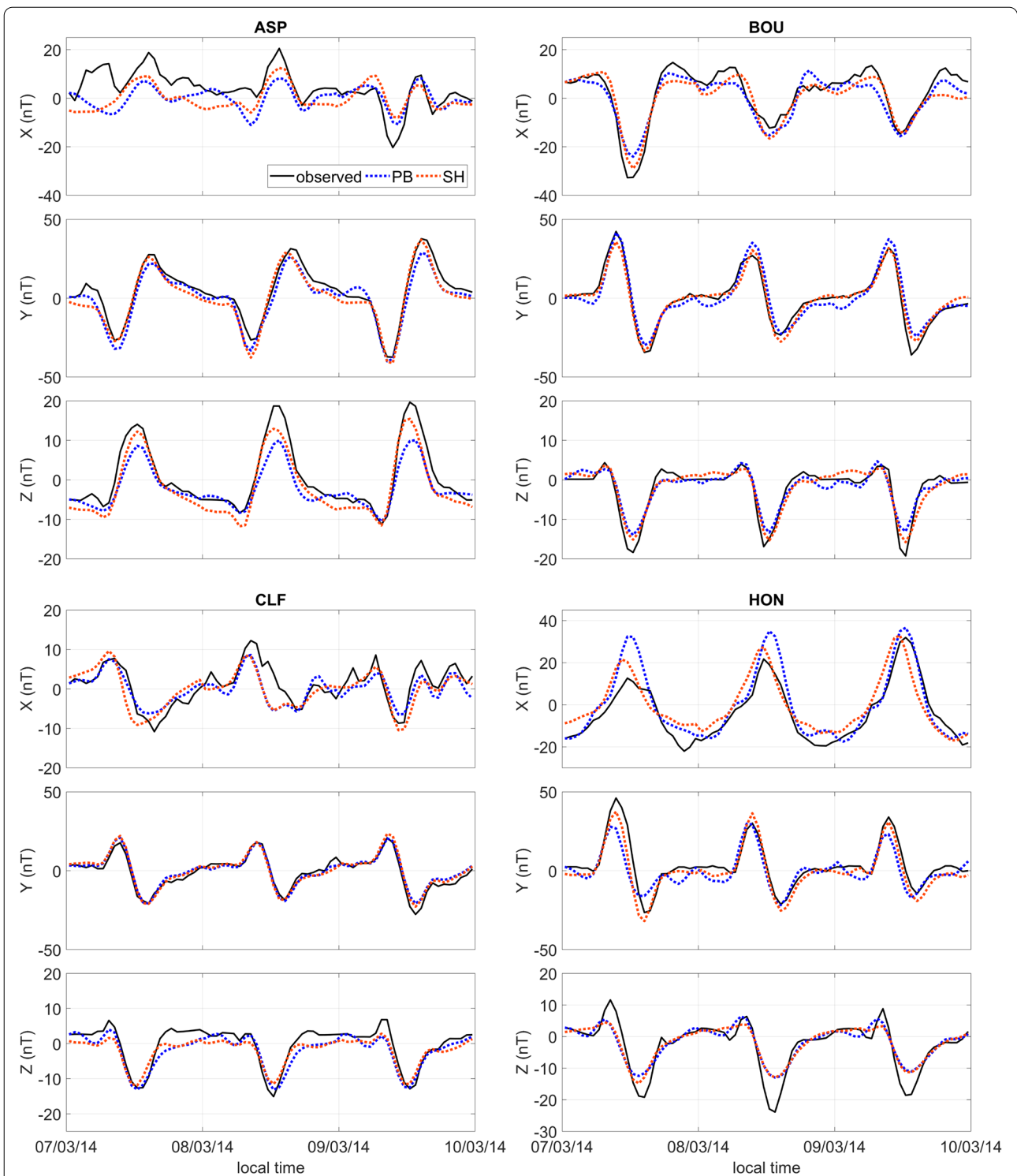
Conclusions

The main goal of the paper was to investigate whether magnetic fields computed in a realistic Earth's 3-D conductivity model excited by a PCA-based source agree better with the observations than those computed in the same model but induced by an SH-based source.

PCA was applied to the Fourier transformed stream function from the physics-based Thermosphere Ionosphere Electrodynamics General Circulation Model

Zenhäusern *et al. Earth, Planets and Space*   (2021) 73:136

Page 14 of 16

Fig. 11 Comparison of observed (black) and predicted magnetic field components *X*, *Y*, and *Z*. Predictions using the physics-based and SH parameterization are given by the blue and red dashed lines, respectively. Shown are the results for observatories ASP, BOU, CLF, and HON for a period between March 8th and March 14th, 2014. SH results are from Guzavina et al. (2019). Note the different *y*-axis scales

of Atmosphere and Ionosphere for Aeronomy [GAIA; Jin et al. (2011, 2012), Fujita et al. (2018)] could be used to investigate this problem further.

Abbreviations

3-D: Three-dimensional; AEJ: Auroral Electrojet; EM: Electromagnetic EEJ: Equatorial Electrojet; GAIA: Ground-to-topside model of Atmosphere and Ionosphere for Aeronomy; G2L: Global-to-local; GDS: Geomagnetic Depth Sounding; FT: Fourier transform; MTZ: Mantle Transition Zone; PC: Principal Component; PCA: Principal Component Analysis; Sq: Solar quiet; TIE-GCM: Thermosphere Ionosphere Electrodynamics General Circulation; UM: Upper Mantle.

Authors' contributions

GZ processed and analyzed the modeled and observatory data. MG provided the code to estimate external coefficients. AM performed TIE-GCM modeling. AK created the concept of the study and provided the 3-D modeling code X3DG. GZ drafted the manuscript. All authors read and approved the final manuscript.

Availability of data and materials

The data sets analysed during the current study are available in the UCAR/NCAR—DASH Repository, with the identifier https://doi.org/10.5065/akxe-2a56 (Maute 2020).

Declarations

Competing interests

The authors declare that they have no competing interests.

Author details

[1]Institute of Geophysics, ETH Zurich, Sonneggstrasse 5, 8092 Zurich, Switzerland. [2]High Altitude Observatory, National Center for Atmospheric Research, Boulder, CO, USA.

References

Alken P, Maute A, Richmond AD, Vanhamäki H, Egbert GD (2017) An application of principal component analysis to the interpretation of ionospheric current systems. J Geophys Res Space Phys 122(5):5687–5708. https://doi.org/10.1002/2017JA024051

Aster RC, Borchers B, Thurber CH (2018) Parameter estimation and inverse problems. Elsevier, Amsterdam

Björnsson H, Venegas S (1997) A manual for EOF and SVD analyses of climatic data. CCGCR Rep 97(1):112–134

Chulliat A, Blanter E, Le Mouël JL, Shnirman M (2005) On the seasonal asymmetry of the diurnal and semidiurnal geomagnetic variations. J Geophys Res Space Phys. https://doi.org/10.1029/2004JA010551

Egbert GD, Alken P, Maute A, Zhang H, Richmond AD (2020) Modeling diurnal variation magnetic fields for mantle induction studies. Geophys J Int. https://doi.org/10.1093/gji/ggaa533

Emery BA, Roble RG, Ridley EC, Richmond AD, Knipp DJ, Crowley G, Evans DS, Rich FJ, Maeda S (2012) Parameterization of the ion convection and the auroral oval in the NCAR Thermospheric General Circulation Models. Tech. Rep. No. NCAR/TN-491+STR, National Center for Atmospheric Research, Boulder CO, USA, https://doi.org/10.5065/D6N29TXZ

Fujita S, Murata Y, Fujii I, Miyoshi Y, Shinagawa H, Jin H, Fujiwara H (2018) Evaluation of the Sq magnetic field variation calculated by GAIA. Space Weather 16(4):376–390. https://doi.org/10.1002/2017SW001745

Grayver A, Munch FD, Kuvshinov A, Khan A, Sabaka TJ, Tøffner-Clausen L (2017) Joint inversion of satellite-detected tidal and magnetospheric signals constrains electrical conductivity and water content of the upper mantle and transition zone. Geophys Res Lett 44(12):6074–6081

Guzavina M, Grayver A, Kuvshinov A (2018) Do ocean tidal signals influence recovery of solar quiet variations? Earth Planets Space 70(1):1–15. https://doi.org/10.1186/s40623-017-0769-1

Guzavina M, Grayver A, Kuvshinov A (2019) Probing upper mantle electrical conductivity with daily magnetic variations using global to local transfer functions. Geophys J Int 219(3):2125–2147. https://doi.org/10.1093/gji/ggz412

Häusler K, Lühr H, Hagan ME, Maute A, Roble RG (2010) Comparison of CHAMP and TIME-GCM nonmigrating tidal signals in the thermospheric zonal wind. J Geophys Res Atmos. https://doi.org/10.1029/2009JD012394

Heelis RA, Lowell JK, Spiro RW (1982) A model of the high-latitude ionospheric convection pattern. J Geophys Res Space Phys 87(A8):6339–6345. https://doi.org/10.1029/JA087iA08p06339

Jin H, Miyoshi Y, Fujiwara H, Shinagawa H, Terada K, Terada N, Ishii M, Otsuka Y, Saito A (2011) Vertical connection from the tropospheric activities to the ionospheric longitudinal structure simulated by a new earth's whole atmosphere-ionosphere coupled model. J Geophys Res Space Phys. https://doi.org/10.1029/2010JA015925

Jin H, Miyoshi Y, Pancheva D, Mukhtarov P, Fujiwara H, Shinagawa H (2012) Response of migrating tides to the stratospheric sudden warming in 2009 and their effects on the ionosphere studied by a whole atmosphere-ionosphere model GAIA with COSMIC and TIMED/SABER observations. J Geophys Res Space Phys. https://doi.org/10.1029/2012JA017650

Koch S, Kuvshinov A (2013) Global 3-D EM inversion of Sq variations based on simultaneous source and conductivity determination: concept validation and resolution studies. Geophysical Journal International 195(1):98–116, http://academic.oup.com/gji/article/195/1/98/601438/Global-3D-EM-inversion-of-Sq-variations-based-on

Kuvshinov A (2008) 3-D global induction in the oceans and solid earth: recent progress in modeling magnetic and electric fields from sources of magnetospheric, ionospheric and oceanic origin. Surv Geophys 29:139–186. https://doi.org/10.1007/s10712-008-9045-z

Maute A (2017) Thermosphere-ionosphere-electrodynamics general circulation model for the ionospheric connection explorer: TIEGCM-ICON. Space Sci Revi 212(1–2):523–551

Maute, Astrid. (2020). Ground magnetic perturbation due to external ionospheric current for a solar minimum and maximum year. Version 1.0. UCAR/NCAR - DASH Repository. https://doi.org/10.5065/akxe-2a56. https://dashrepo.ucar.edu/dataset/141_maute.html. Accessed 01 Feb 2021.

Maute A, Richmond AD (2017a) Examining the magnetic signal due to gravity and plasma pressure gradient current with the tie-gcm. J Geophys Res Space Phys 122(12):12,486-12,504. https://doi.org/10.1002/2017JA024841

Maute A, Richmond AD (2017b) F-region dynamo simulations at low and mid-latitude. Space Sci Rev 206(1):471–493. https://doi.org/10.1007/s11214-016-0262-3

Olsen N (1991) Untersuchung von tagesperiodischen Variationen des Erdmagnetfeldes mit neueren statistischen Methoden. PhD Thesis, Georg-August-Universität zu Göttingen

Pankratov O, Kuvshinov A (2016) Applied mathematics in EM studies with special emphasis on an uncertainty quantification and 3-D integral equation modelling. Surv Geophys 37(1):109–147

Püthe C, Kuvshinov A, Olsen N (2015) Handling complex source structures in global EM induction studies: from C-responses to new arrays of transfer functions. Geophys J Int 201(1):318–328

Zenhäusern *et al. Earth, Planets and Space*   *(2021) 73:136*

Page 16 of 16

Qian L, Burns AG, Emery BA, Foster B, Lu G, Maute A, Richmond AD, Roble RG, Solomon SC, Wang W (2014) The NCAR TIE-GCM, American Geophysical Union (AGU), chap 7, pp 73–83. https://doi.org/10.1002/9781118704417.ch7

Roble RG, Ridley EC, Richmond AD, Dickinson RE (1988) A coupled thermosphere/ionosphere general circulation model. Geophys Res Lett 15(12):1325–1328. https://doi.org/10.1029/GL015i012p01325

Schmucker U (1999) A spherical harmonic analysis of solar daily variations in the years 1964–1965: response estimates and source fields for global induction-I. Methods. Geophys J Int 136:439–454. https://doi.org/10.1046/j.1365-246X.1999.00742.x

Yamazaki Y, Maute A (2017) Sq and EEJ-A review on the daily variation of the geomagnetic field caused by ionospheric dynamo currents. Space Sci Rev 206(1–4):299–405. https://doi.org/10.1007/s11214-016-0282-z

Yamazaki Y, Yumoto K, Cardinal MG, Fraser B, Hattori P, Kakinami Y, Liu J, Lynn K, Marshall R, Mcnamara D, Nagatsuma T, Nikiforov V, Otadoy RE, Ruhimat M, Shevtsov B, Shiokawa K, Abe S, Uozumi T, Yoshikawa A (2011) An empirical model of the quiet daily geomagnetic field variation. J Geophys Res. https://doi.org/10.1029/2011JA016487

Publisher's Note

Springer Nature remains neutral with regard to jurisdictional claims in published maps and institutional affiliations.